Materialia 18 (2021) 101159

Contents lists available at ScienceDirect

Materialia

journal homepage: www.elsevier.com/locate/mtla

Full Length Article

Tracing plastic deformation path and concurrent grain refinement during additive friction stir deposition

Mackenzie E.J. Perry[a,b], Hunter A. Rauch[a], R. Joey Griffiths[a], David Garcia[a], Jennifer M. Sietins[b], Yunhui Zhu[c], Yuntian Zhu[d], Hang Z. Yu[a,*]

[a] Department of Materials Science and Engineering, Virginia Tech, Blacksburg VA 24061, USA
[b] CCDC Army Research Laboratory, Aberdeen Proving Ground, Aberdeen MD 21005, USA
[c] Department of Electrical and Computer Engineering, Virginia Tech, Blacksburg VA 24061, USA
[d] Department of Materials Science and Engineering, City University of Hong Kong, 83 Tat Chee Ave, Kowloon Tong, Hong Kong, China

ARTICLE INFO

Keywords:
Additive friction stir deposition
X-ray computed tomography
Severe plastic deformation
Dynamic recrystallization
Aluminum alloys

ABSTRACT

Owing to melting and solidification, serious issues arise in fusion-based metal additive manufacturing, such as solidification porosity, columnar grains, and large grain sizes. Recently, additive friction stir deposition has been demonstrated to overcome these issues via high-temperature, rapid plastic deformation, which can result in fully-dense as-printed material with equiaxed, fine grains. However, the deformation fundamentals underlying this process—e.g., the strain magnitude, its influence on dynamic microstructure evolution, and material flow details—remain poorly understood. Here, we explore the deformation fundamentals of additive friction stir deposition by employing tracer-based feed material (Al-Cu tracer embedded in Al-Mg-Si matrix). This allows us to unravel: (i) the path of plastic deformation, and (ii) concurrent grain structure evolution along the deformation path. X-ray computed tomography is used to directly observe the plastic deformation paths of center and edge tracers. In both cases, the millimeter-scale cylindrical tracer undergoes extrusion- and torsion-like deformation followed by shear-induced thinning, which eventually results in micro-ribbons piling up along the deposition track. Microstructure mapping along the deformation path reveals significant grain refinement during initial material feeding via geometric dynamic recrystallization but no further grain refinement during steady-state deposition. By analyzing the strain components associated with extrusion, torsion, and shear-induced thinning, we estimate the total strain to be on the order of 10^1 and establish a quantitative relationship between the strain and tracer grain size. While this work focuses on a specific process, the methodology and findings may provide the basis for developing future deformation processing-based additive technologies.

1. Introduction

Metal additive manufacturing traditionally involves selective melting of powders via a laser or an electron beam [1-3], wherein the print quality, microstructure, and properties are governed by rapid solidification [2]. Owing to the nature of melting and solidification, fundamental challenges persist despite extensive research, including solidification-induced porosity [4, 5], large thermal gradients and residual stresses [6, 7], columnar grain structure formation [8], risk of hot cracking [9], as well as the large energy consumption by high-power beam sources [10]. In conventional metal manufacturing like casting, most of these issues are also present and are often addressed by subsequent deformation processing, e.g., forging or rolling, which is capable of removing the casting porosity, modifying or refining the microstructure, and improving the mechanical performance [11]. Such advantages have motivated researchers to develop alternative additive manufacturing routes that utilize plastic deformation, rather than melting and solidification, to enable interface bonding [12, 13]. Examples include ultrasonic additive manufacturing [14-16], cold spray additive manufacturing [17-19], and additive friction stir deposition (AFSD) [20, 21]. The former two only involve local plastic deformation [12] (i.e., at the layer interface or particle contact), whereas AFSD is characterized by global deformation in which the entire feed material is stirred at elevated temperatures. Given this propensity for deformation processing, AFSD is able to produce fully-dense *as-printed* material with equiaxed, fine microstructures [22-25] and wrought-like mechanical properties [26-28]—a unique capability distinguishing it from other metal additive processes [29].

In AFSD, the principle of friction stirring is applied in the context of additive manufacturing to enable rapid heating and deformation of metals [30]. During *initial material feeding*, the feed-rod rotates rapidly with the tool head while being slowly fed towards the substrate. Shortly af-

* Corresponding author.
E-mail address: hangyu@vt.edu (H.Z. Yu).

https://doi.org/10.1016/j.mtla.2021.101159
Received 22 April 2021; Accepted 5 July 2021
Available online 13 July 2021

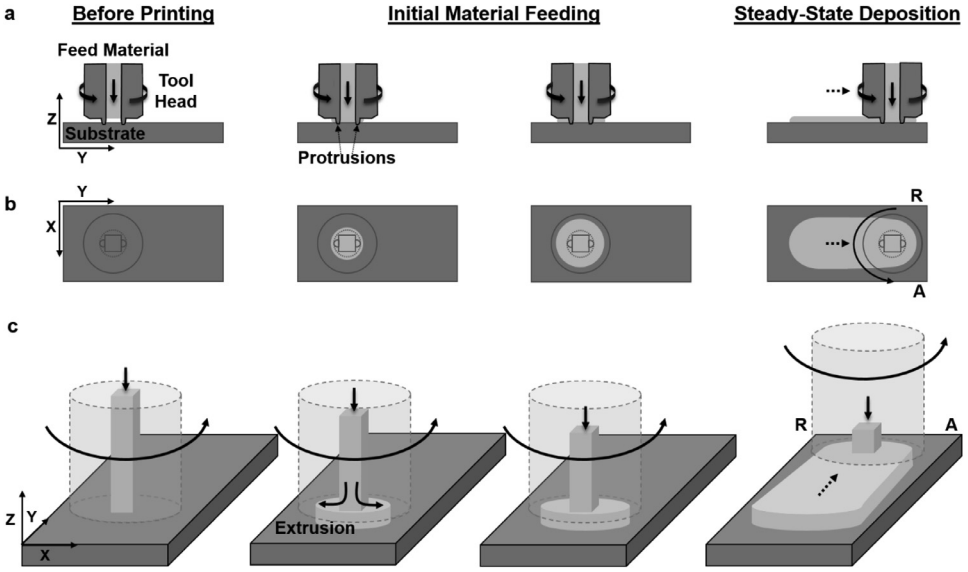

Fig. 1. Schematics of the main processing steps in additive friction stir deposition (from left to right): before printing, during initial material feeding, and during steady-state deposition. This includes (a) side view, (b) top view, and (c) isometric view. The protrusions at the tool bottom surface are designed to promote material flow. The X-, Y-, and Z-axes refer to the transverse, longitudinal, and normal directions, respectively, following the right-hand rule. The positive X-direction is defined from the retreating side (R) to the advancing side (A). The positive Y-direction is in the traveling direction of tool head.

ter reaching the substrate, the feed-rod reaches an elevated temperature due to frictional heating, and then it yields and extrudes to fill the space between the rotating tool head and substrate. In this processing step, friction stirring not only plastically deforms the deposited material, but also the substrate surface, resulting in metallurgical bond formation and a non-planar interface with complex 3D features [22]. Once the actuation force and torque stabilize, the system is ready for *steady-state deposition*. The material feed rate is then increased and the tool head starts to move in-plane to create a material pattern guided by a G-code. Fig. 1 illustrates the main processing steps in AFSD, including the scenarios before printing, during initial material feeding, and during steady-state deposition.

The last few years have witnessed vigorous research activities in the AFSD field, including process physics [22, 31], microstructure analysis [23-25, 27, 32-34], static and fatigue properties [26, 28, 35-39], as well as niche engineering applications (e.g., additive repair [40], automotive cladding [41], and material recycling [42]). As a deformation-based approach for metal additive manufacturing, however, the underlying fundamentals are still far from well understood in AFSD. Several critical questions remain:

- What is the strain magnitude? As a friction stir-related process, the strain in AFSD is expected to be large [43-45], but there is a lack of quantitative assessment giving concrete numerical values. Because the deformation in AFSD is rapid and is intrinsically coupled with heat transfer and generation, it is challenging to calculate the strain by the number of revolutions or the geometry of sample and tool as seen in static severe plastic deformation literature [46-49].
- What is the material deformation path? Is the deformation uniform across all mesoscopic material domains in the feed-rod? The answers to these questions are vital for assessing strain accumulation in AFSD. From a materials design perspective, the large plastic deformation in AFSD facilitates the formation of heterostructured materials [50] with complex architectures, the geometry of which can only be controlled by understanding the material deformation paths [51].
- What are the influences of plastic deformation on microstructure evolution *during* AFSD? Although the microstructures before and after AFSD have been compared in a number of materials [22-25, 32], the microstructural changes in the transitional steps (e.g., when the material initially exits the tool head channel, reaches the substrate, or rotates under the tool head) have remained elusive. This has prevented robust control of the microstructure and its spatial distribution in the as-printed material.

To address these questions, here we explore the deformation fundamentals of AFSD through complementary studies on the (i) deformation path of feed material and (ii) concurrent dynamic microstructure evolution. In this context, deformation is not only on the macroscopic level, i.e., changing from a feed-rod to a thin material disc by extrusion, but also—and more importantly—on the mesoscopic level. Inspired by material flow studies in friction stir welding [52-54], we employ tracer-based feed-rods and analyze how the tracer deforms, stretches, or flattens during deposition using X-ray computed tomography. In this work, we specifically choose an Al-Cu alloy (AA2024) as the tracer, which is embedded into the matrix made of an Al-Mg-Si alloy (AA6061). This pair of Al alloys is chosen because they can be distinguished in X-ray imaging [22] and they have comparable mechanical properties at elevated temperatures. This prevents substantial tracer fragmentation during friction stirring [55, 56] and allows for strain quantification.

Whether the tracer is in the center or close to the edge of the feed-rod, the original millimeter-scale cylindrical shape is seen to be transformed into a series of micro-ribbons (thickness ~ tens of μm) that pile up along the deposition track, providing direct evidence for severe plastic deformation. Microstructure mapping along the tracer deformation path shows significant grain refinement via geometric dynamic recrystallization shortly after the feed material exits the tool head channel. Despite large strain accumulation during the remainder of steady-state deposition, the grain size is not further reduced. By analyzing the tracer shape changes at various deformation steps, we quantify the strain during AFSD and establish a quantitative relationship between the grain size and the strain, which is shown to be consistent with the recrystallization mechanism identified in microstructural analysis. Although the focus is on a specific process, AFSD, the approach and discoveries in this work can be useful for developing other deformation processing-based additive technologies in the future.

2. Experimental procedures

2.1. Material deposition by AFSD

The material deposition by AFSD was conducted using a MELD R2 machine [57] (MELD Manufacturing Corporation, Christiansburg, VA, USA) outfitted with an H13 steel tool head. The tool head had an outer diameter of 38 mm with two small, rounded protrusions on the bottom surface directly adjacent to the central channel opening. As detailed in

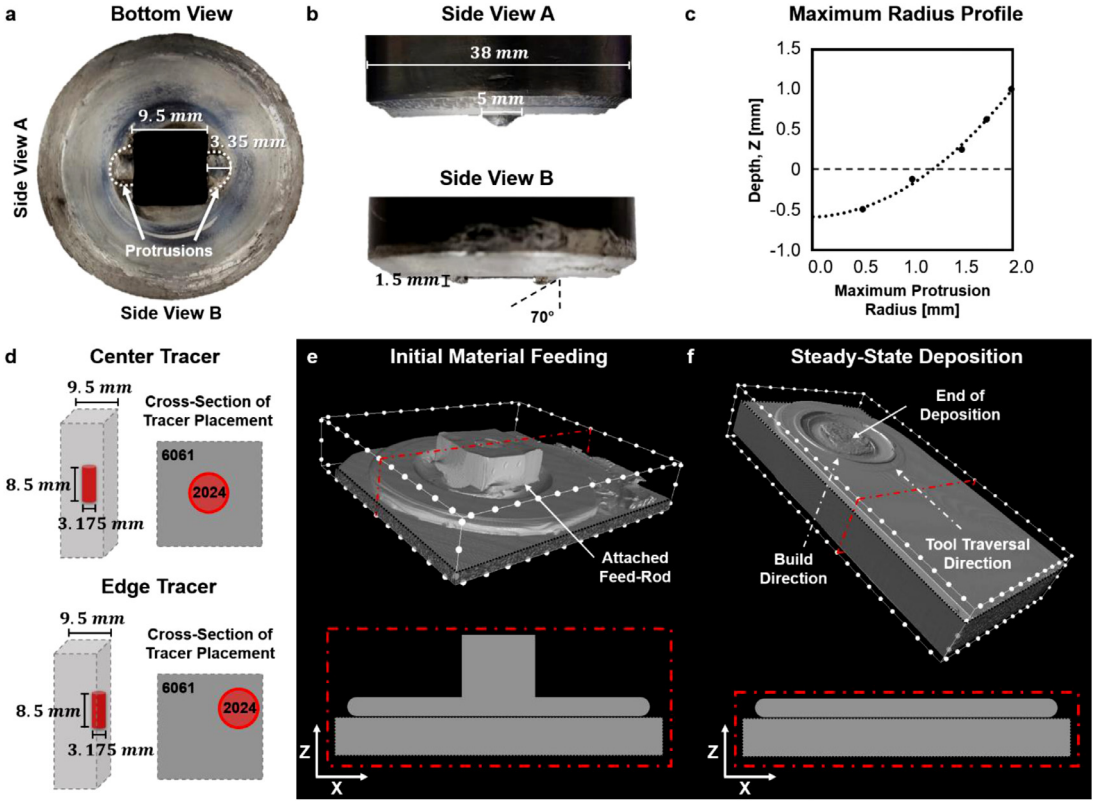

Fig. 2. Experimental details. Geometry of the protrusions: (a) bottom view, (b) side views, and (c) plot of the protrusion profile. Here, the height of the substrate surface before printing is defined as Z = 0 mm. (d) Experimental design, showing the geometry of two types of hybrid feed-rods with the AA2024 tracer placed in the center or close to the edge of the AA6061 matrix. For each type of deposition, X-ray computed tomography and microstructure characterization are performed for two scenarios: (e) after initial material feeding and (f) after steady-state deposition. In (e) and (f), the red dashed lines indicate the cross-section used for microstructure analysis; the distance between each pair of white dots is 2.5 mm.

Figs. 2(a)-(c), the protrusions have a curved shape with the outermost radius increasing with the Z-height. From the side view, the profile of the protrusions forms an angle of 70° with respect to the vertical direction. During printing, these surface protrusions were partially inserted into the substrate to generate additional heat and enhance material flow and mixing [31]. The importance of protrusions in AFSD is further discussed in Section 3.2, in the context of material thinning caused by material-protrusion interactions.

To understand the deformation paths of mesoscopic domains in the feed material, customized hybrid feed-rods were employed. Each feed-rod consisted of an AA6061 matrix (square cross-section of 9.535 mm × 9.535 mm) and an AA2024 tracer core (cylindrical shape; diameter of 3.175 mm and length of 8.5 mm). An AA6061 plate of 6.35 mm thick was used as the substrate. The tracer was either placed in the center or close to the edge of the feed-rod, as illustrated in Fig. 2(d), allowing us to understand the deformation paths of the center and edge domains in the feed-rod. For each type of hybrid feed-rod (center tracer or edge tracer), the material flow pattern and microstructure evolution were investigated after initial material feeding and after steady-state material deposition. During initial material feeding, the rotation rate was set at 300 RPM (revolution per minute) and the feed rate was set at 0.06 mm/s. The initial material feeding experiments were ended abruptly to keep the remaining feed-rod attached (Fig. 2(e)). During steady-state material deposition (Fig. 2(f)), the rotation rate stayed the same, the feed rate was increased to 0.85 mm/s, and the in-plane velocity was set at 2.54 mm/s. These process parameter values were selected as they were proven to ensure good print quality. The current AFSD facility was designed for large-scale additive manufacturing with a deposition layer thickness of 1 mm and an average track width of 28.5 mm.

2.2. X-ray micro-computed tomography

The 3D shape of the tracer was studied using X-ray computed tomography after initial material feeding and after steady-state material deposition. For global material shape information, the entirety of each sample was scanned using an X5500 3D X-ray inspection system (North Star Imaging, Rogers, MN, USA) with the voxel size in the range of 33.1-43 μm, the voltage in the range of 120-180 kV, and the current in the range of 275-800 mA. To investigate local regions for more details, a micro-waterjet was used to create smaller specimens measuring 30 mm × 6 mm × 8 mm. Such smaller samples were scanned using an Xradia 520 Versa MicroCT system (Zeiss, Oberkochen, Germany) at higher resolution; the voxel size was in the range of 3.57- 9.85 μm at a voltage of 60 kV and a current of 83 mA. The reconstructed volumes were visualized using CTVox software (Bruker, Billerica, MA, USA).

2.3. Microstructure characterization

The cross-sections for microstructure characterization are highlighted by red dashed lines after initial material feeding (Fig. 2(e)) and after steady-state deposition (Fig. 2(f)). In the initial material feeding case, the cross-section was cut along the centerline of the feed-rod. All samples were ground with 400, 600, and 1200 grit silicon carbide papers, followed by 6 µm, 3 µm, and 1 µm polycrystalline diamond suspensions, and finished with a 0.02 µm colloidal silica suspension. The central facility for microstructure characterization was a NOVA NanoSEM 600 field emission scanning electron microscope (FEI Company, Hillsboro, OR, USA), which was equipped with an Octane Elite energy dispersive spectroscopy (EDS) detector and an electron backscatter diffraction (EBSD) detector. For EBSD mapping, step sizes ranged from 0.08-2

μm depending on the size of the scanned area. Boundary misorientations from 2° to 15° were classified as low angle boundaries (LABs), while boundary misorientations above 15° were identified as high angle boundaries (HABs). The EBSD scan data was analyzed using OIM Analysis (EDAX, Mahwah, NJ, USA). The maps constructed from the scan data included inverse pole figure (IPF) maps, misorientation maps, kernel average misorientation (KAM) maps, and grain average misorientation (GAM) maps. The average grain size was determined by averaging the area of all identified grains followed by calculating the circle equivalent diameter.

3. Material deformation path revealed by X-ray computed tomography

3.1. Initial material feeding: extrusion- and torsion-like deformation

Fig. 3 shows the X-ray computed tomography results after initial material feeding, wherein the hybrid feed-rod is connected to the deposit. Z = 0 mm and Z = 1 mm correspond to the height of the initial substrate surface and the bottom of the tool head, respectively. For the center tracer (Figs. 3(a)-(c)), the cylindrical shape is maintained until Z ~ 0.5 mm. Moving down along the Z-direction, the X-Y plane cross-sectional area is seen to increase due to extrusion of the feed material. In 3D space, the center tracer develops into a corkscrew shape (upside-down view in Fig. 3(c)). For the edge tracer (Figs. 3(d)-(f)), the original cylinder develops into a helix throughout the entire volume of the feed-rod. Even when the edge tracer is constrained in the tool head (Z > 1 mm), it is seen to tilt in the X-Z plane (Fig. 3(d)) and twist in the isometric view (Fig. 3(f)).

Within the tool head channel, the rotation rate of the feed-rod is defined by the tool head (300 RPM). At the substrate surface level, the rotation rate drops significantly as the material co-deforms and mixes with the non-rotating substrate surface. Between the tool head and substrate, therefore, there is a gradual decrease of the rotation rate along the Z-direction. A combination of this rotation rate gradient and downward material feeding results in helical-type shape evolution for both the center and edge tracers. The difference lies in the rotation radius and mechanical constraint. For the center tracer, the rotation axis is the same as the tool head, and the tracer is mechanically constrained by the surrounding matrix material. The helical-type shape evolution is thus constrained by the radius of the original tracer cylinder, resulting in its tight corkscrew appearance. The edge tracer has a much larger radius of rotation with less matrix material impeding its motion, which results in more significant shape evolution as seen by the helix.

To summarize, at least two strain components should be considered during initial material feeding. First, there is an extrusion strain due to compression on the feed-rod, which causes cross-sectional area changes. Second, there is a torsional strain resulting from the rotation rate gradient, which causes helical-type shape formation. These strain components are quantitatively analyzed in Section 5.1.1.

3.2. Steady-state deposition: transformation to micro-ribbons

Fig. 4 presents the high-resolution X-ray computed tomography results after steady-state deposition, in which the AA2024 tracer is depicted in red and the surrounding AA6061 matrix is made transparent. For both center (Figs. 4(a)-(c)) and edge (Figs. 4(d)-(f)) tracers, the initial millimeter-scale cylinder is remarkably transformed into curved micro-ribbons with a thickness on the order of tens of microns. From X-ray imaging, the average thickness for the micro-ribbons formed by the center tracer is measured to be 27.8 μm; this is close to that measured by microstructure analysis, 27.5 μm (see Section 4). These micro-ribbons are likely formed by a significant thinning process associated with large shear deformation. Figs. 4(c) and (f) show the Y-Z plane view: the micro-ribbons tilt ~ 70° along the Y-direction and approximately resemble the

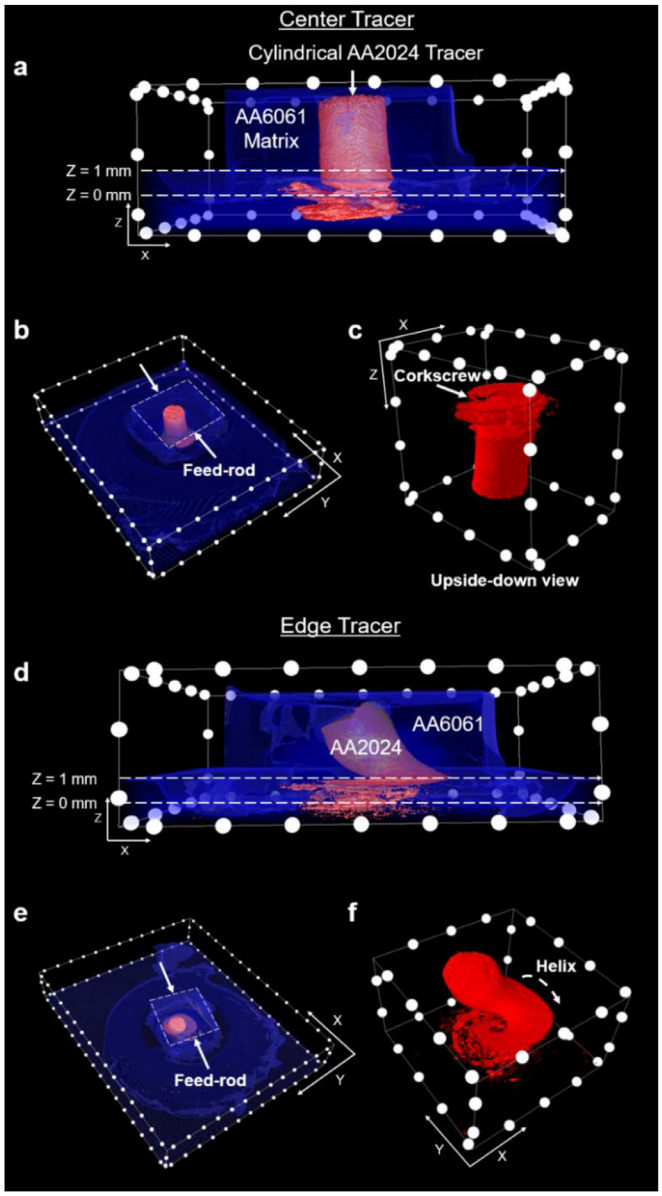

Fig. 3. X-ray computed tomography results after initial material feeding for the ((a)-(c)) center tracer and ((d)-(f)) edge tracer. The AA2024 tracer is depicted in red and the surrounding AA6061 matrix is either in blue or transparent. The distance between each pair of white dots is 2.5 mm.

shape of the tool protrusions (recall Fig. 2), suggesting a linkage between the micro-ribbon formation and material-protrusion interactions in AFSD.

In friction stir welding or FSW, severe material thinning caused by material-pin interactions has been widely reported. Using a soft and ductile aluminum foil (AA5457) as the tracer in a workpiece (AA5083), Mukherjee and Ghosh observed a progressive thinning of the foil on the retreating side as the foil was sheared by the pin [55]. The original thickness of the foil was ~ 290 μm, whereas after FSW, the thickness of the foil was measured to be ~ 3 μm. With the material-pin interactions, the dimension in the thickness direction was reduced by two orders of magnitude. Liu *et al.* examined the strain development in FSW of Cu containing a Cu-40Zn foil marker that was 500 μm thick [44]. After welding, the thinnest region of the foil was reduced to 11.5 μm, which is slightly less than two orders of magnitude reduction from the original thickness. In the present work of AFSD, no pin is used, but the two small protrusions on the bottom surface of the tool can play a similar role in shear

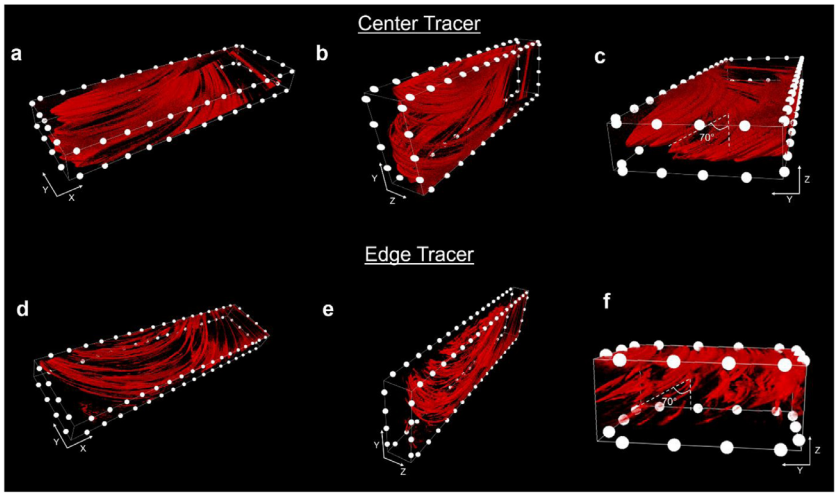

Fig. 4. High-resolution X-ray computed tomography results after steady-state deposition for ((a)-(c)) center tracer and ((d)-(f)) edge tracer. The distance between each pair of dots is 1.25 mm.

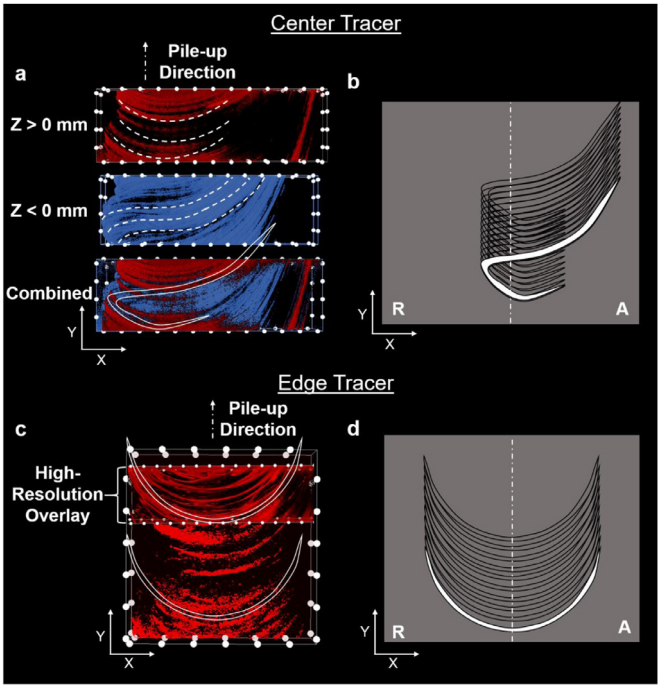

Fig. 5. Shapes of the micro-ribbons after steady-state deposition. (a) Micro-ribbons of two segments resulting from the center tracer, showing the top portion (Z > 0 mm), bottom portion (Z < 0 mm), and a combined image. The distance between each pair of dots is 1.25 mm. (b) Illustration of the pile-up of the micro-ribbons along the deposition track for the center tracer experiment. (c) Micro-ribbons of a long arch shape resulting from the edge tracer. The distance between each pair of dots is 2.5 mm for the lower resolution, global-scale image and 1.25 mm for the higher resolution, local volume. (d) Illustration of the pile-up of the micro-ribbons along the deposition track for the edge tracer experiment. R and A refer to the retreating and the advancing side, respectively.

thinning. The diameter of the original tracer cylinder is 3.175 mm; after shear-induced thinning, the typical width of the micro-ribbons in the X-Y plane is 27.8 μm. This is also a two orders of magnitude reduction of the dimension.

Fig. 5 presents the X-Y plane view of the center and edge tracers after steady-state deposition, clearly showing that the resultant micro-ribbons pile up along the traveling direction of the tool head (i.e., Y-direction). For the center tracer experiment, each micro-ribbon consists of two segments. As shown in Fig. 5(a), the bottom portion (in blue, Z < 0 mm) is longer and extends in the positive Y-direction, finally reaching the advancing edge; the top portion (in red, Z > 0 mm) is shorter and extends toward the opposite direction (negative Y-direction). The curvature of each portion is different; overall, each micro-ribbon exhibits a folded shape that extends in the 3D space. For the edge tracer experiment, each micro-ribbon shape can be best described by a long arch. This is clearly demonstrated in Fig. 5(c), which shows the top view of these micro-ribbons on the global scale. Figs. 5(b) and (d) illustrate the shapes of the micro-ribbons resulting from the center and edge tracers; their pile-up results in a periodic appearance along the deposition track.

4. Concurrent grain refinement in the tracer material

4.1. Initial material feeding: significant grain size reduction

The employment of a tracer material allows us to track the microstructure evolution *during* AFSD. Based on X-ray computed tomography of the center tracer experiment, Fig. 6(a) presents an X-Z cross-sectional slice along the centerline during initial material feeding. Fig. 6(b) shows an IPF map of the original AA2024 tracer material before AFSD; its color legend applies to all IPF maps in this study. Figs. 6(c)-(g) depict the IPF maps for Areas 1-5 labeled in Fig. 6(a). Area 1 is inside the tool head (Z = 4.2 mm); Area 2 is close to the bottom of the tool head (Z = 1.1 mm); Areas 3-5 are all in the deposited material below the tool head, with Z = 0.9, 0.26 and -0.2 mm, respectively. The grain size and shape in Areas 1 and 2 are similar to the original AA2024 tracer, suggesting that the original microstructure of the center tracer is largely preserved when the feed material is still inside the tool head.

Substantial microstructure evolution occurs right after the center tracer leaves the tool head. In Area 3, the grains elongate and thin to ~ 3-5 μm wide, while curving towards the horizontal direction. Further down, such as in Areas 4 and 5, the thin, elongated microstructure has been replaced by fine, equiaxed grains. Notably, from Z = 1.1 mm (Area 2) to Z = 0.26 mm (Area 4), the microstructure of the AA2024 tracer drastically changes, transitioning from vertically elongated, large grains ~ 25-30 μm to small, equiaxed grains with an average size of 1.36 μm. We note that the curving of grains in Area 3 is most likely a manifestation of the torsional strain as discussed in Section 3.1. Nevertheless, this torsional strain should be zero along the rotation axis (i.e., the centerline). This seeming discrepancy could be a result of the weaker constraint and possible horizontal material displacement below Z = 1 mm: the material domain observed in Area 3 may have originated slightly off of the center rotation axis.

Fig. 7 compares the misorientation angle distributions, misorientation maps, and GAM maps for Areas 1-5. The GAM value is an average of the local misorientation present in each neighborhood of EBSD pix-

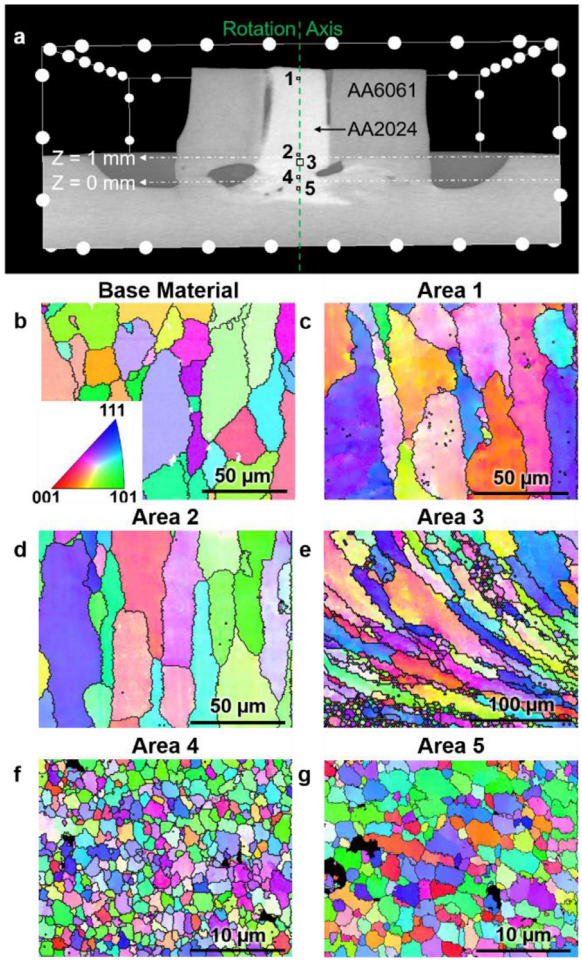

Fig. 6. Grain structure evolution of the center tracer during initial material feeding. (a) The cross-section used for microstructure characterization with areas of interest labeled. Distance between each pair of white dots is 2.5 mm. IPF maps of the AA2024 tracer for (b) before AFSD, (c) Area 1 (Z = 4.2 mm), (d) Area 2 (Z = 1.1 mm), (e) Area 3 (Z = 0.9 mm), (f) Area 4 (Z = 0.26 mm), and (g) Area 5 (Z = -0.2 mm).

els constrained by defined grain boundaries, allowing for a quantitative comparison of intra-granular orientation gradients. This is different from KAM maps, which show the misorientation between each pixel and its immediate neighbors. Areas 1 and 2 exhibit a relatively low fraction of LABs, but from Area 2 to Area 3 the LAB fraction substantially increases from 5.9% to 14.2%. This is accompanied by an increase of the GAM, suggesting the formation of substructures. In Area 4, there is still a notable fraction of LABs, but the GAM is significantly reduced. From Area 4 to Area 5, the LAB fraction decreases from 11.5% to 8.9%, although both areas show fine, equiaxed microstructures. The spatial distribution of microstructural features is relatively uniform in these areas.

4.2. Dynamic recrystallization mechanisms

The significant grain size reduction from Areas 1 and 2 to Areas 4 and 5 is caused by recrystallization, which may be of a continuous or discontinuous type. Discontinuous recrystallization is characterized by 'nucleation' and growth of dislocation-free grains and typically leads to heterogeneous microstructures before recrystallization is complete. This is contradictory to our observation. Continuous dynamic recrystallization (CDRX) does not include discrete nucleation and growth events. It is characterized in part by progressive accumulation, annihilation, and reorganization of dislocations due to concurrent deformation and dynamic recovery, resulting in the formation of subgrains [59]. With further strain development, the misorientation increases, and the subgrain boundaries transition to LABs and eventually to HABs.

The CDRX mechanism well explains the observed microstructure evolution in Figs. 6 and 7. The original AA2024 tracer predominantly consists of HABs, which are preserved in Areas 1 and 2 given the small deformation experienced by the center tracer inside the tool head. When the feed-rod is no longer constrained by the tool head, substantial shear deformation is observed from Area 2 to Area 3, in which more LABs emerge (Fig. 7(h)) as a result of dynamic recovery under high temperature plastic deformation. In Area 4, the thin, elongated grains have evolved to small, equiaxed grains containing LABs, which often completely cut across individual grains. With further deformation, these LABs would become HABs as misorientation increases to more than 15°. This prediction is supported by the observation in Area 5, in which the microstructure mainly consists of HABs. Even in Area 5, dynamic recovery continues to eliminate dislocations and create subgrain boundaries, while deformation continues to create new dislocations and transform subgrain boundaries to LABs and then to HABs. Supporting evidence of subgrain formation in Area 5 can be found in the KAM map in the *Supplementary Materials*.

CDRX in Al alloys typically proceeds via geometric dynamic recrystallization (GDRX) or progressive lattice rotation [60]. A closer scrutiny of the thin, curved grains around Area 3 (see Fig. 8(a)) gives rise to direct evidence of GDRX. GDRX is characterized by the formation of thin, elongated grains with serrated HABs that pinch off to create equiaxed, subgrain-sized grains. In the region highlighted in Figs. 8(b) and (c), seven grains of similar crystallographic orientations are seen to form from the same original elongated grain, which has been sheared to a thickness comparable to the subgrain size. The left three and the right three are small, equiaxed grains separated by LABs, and their size is comparable to those observed in Area 5. The middle grain, however, is still elongated with serrated HABs and a color gradient; it would break into several more equiaxed grains by pinch-off upon further deformation. This observation is consistent with the previous works on AFSD of AA6061 [32] and friction surfacing of AA6082 [61], in which GDRX is also identified as a major recrystallization mechanism.

In addition to the center tracer characterization, we track the microstructure evolution of the edge tracer (detailed in the *Supplementary Materials*). Even inside the tool head at Z = 1.1 mm, horizontally elongated grains start to appear as a result of deformation. This is consistent with the X-ray computed tomography results in Section 3.1, which show that the edge tracer undergoes considerable deformation before leaving the tool head. After that, the edge tracer is seen to develop fine, equiaxed grains due to dynamic recrystallization—similar to the case of the center tracer. To summarize, Figs. 8(d) and (e) plot the grain size and LAB fraction as a function of the Z-height during initial material feeding for the center and edge tracers. In both cases, the grain size is significantly reduced shortly after the material leaves the tool head. This is accompanied by an initial increase of the LAB fraction, suggesting the vital role of CDRX in AFSD of AA2024. The LAB fraction eventually decreases as the recrystallization becomes more complete.

4.3. Steady-state deposition: microstructure characterization along the micro-ribbons

We next characterize the microstructure of the tracer after steady-state deposition, i.e., after the millimeter-scale cylinder has been transformed into a series of micro-ribbons. For the center tracer deposition, Fig. 9(a) shows a slice image of the X-Z cross-section based on X-ray computed tomography, in which the AA2024 micro-ribbons appear as an incomplete oval (bright line). This is essentially a projection image of the curved micro-ribbons seen in Fig. 4(a)-(c). Figs. 9(b)-(m) present the EDS, IPF, and misorientation maps of four representative areas along the oval, which are labeled in Fig. 9(a). The alloy AA2024 has a higher percentage of alloying elements, notably 3.8–4.9 % copper, which trans-

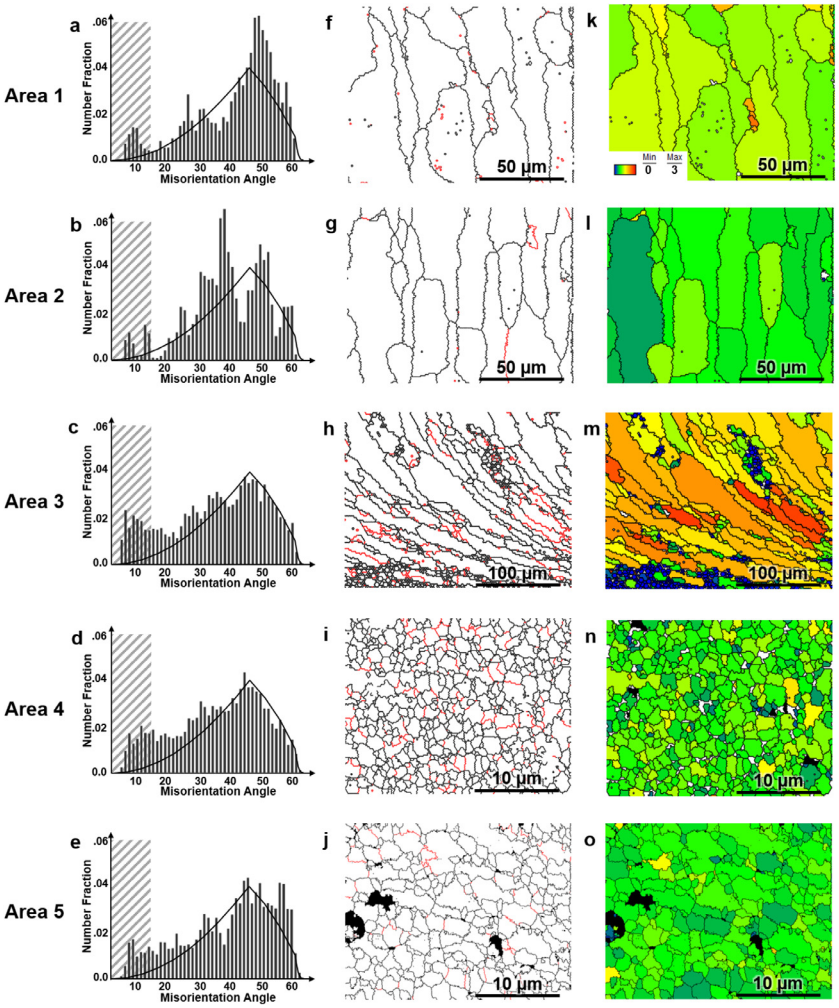

Fig. 7. Detailed comparison of the microstructural features for Areas 1-5. (a)-(e): Misorientation angle distribution with the black line depicting the Mackenzie distribution for a randomly textured polycrystal [58]. (f)-(j): Misorientation maps where LABs are in red and HABs are in black. (k)-(o): Grain average misorientation (0 – 3°) maps.

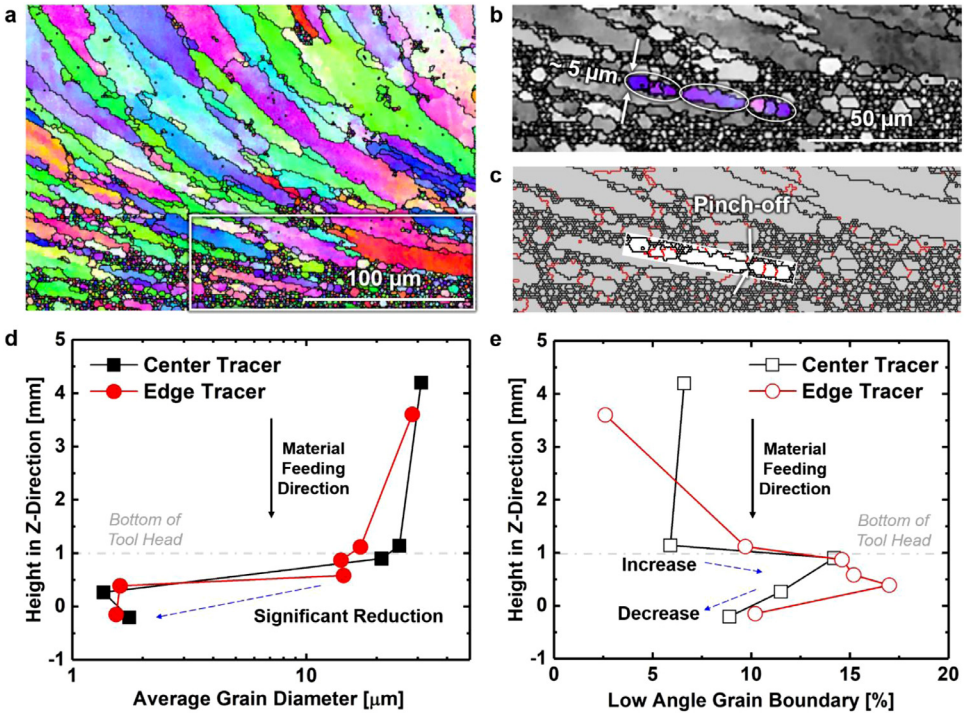

Fig. 8. Mechanisms and trends for microstructural evolution. (a)-(c): Direct evidence of geometric dynamic recrystallization during AFSD of AA2024. (a) An IPF map showing transition of elongated grains to equiaxed grains. Enlarged (b) IPF map and (c) misorientation map for the area of interest boxed in (a). (d)-(e): Quantitative assessment of microstructure evolution of the tracer material. Plots of (d) grain size and (e) LAB fraction against Z-height during initial material feeding, showing data from both center and edge tracers.

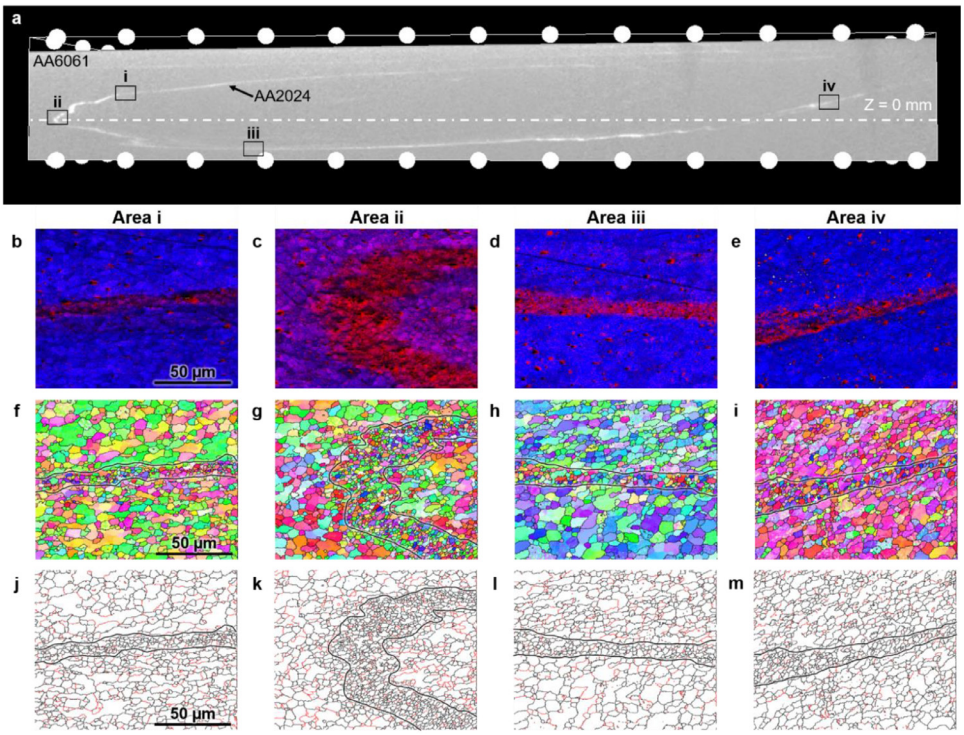

Fig. 9. Microstructure of the center tracer after steady-state deposition. (a) An X-Z cross-sectional image based on X-ray computed tomography, showing the AA2024 as an incomplete oval with four areas of interest labeled. Distance between each pair of dots is 1.25 mm. (b)-(e) EDS maps of the four areas; red indicates lower Al counts corresponding to AA2024, while blue or purple indicates higher Al counts corresponding to AA6061. (f)-(i) IPF maps; the boundaries between the AA2024 tracer and AA6061 matrix are shown as black lines. (j)-(m) Misorientation maps with LABs in red and HABs in black.

lates to fewer aluminum counts than the alloy AA6061. Based on the Al element counts, the EDS maps show areas of higher (in blue or purple) and lower (in red) Al content. This effectively distinguishes the AA2024 tracer (in red) and the AA6061 matrix (in blue or purple); the boundaries between the two materials are highlighted in the IPF and misorientation maps. The average thickness of the AA2024 ribbon is measured to be 27.5 μm.

Although Areas i-iv correspond to characteristically different locations along the tracer oval, the microstructure of the AA2024 tracer is always characterized by fine, equiaxed grains with low fractions of LABs. The grain size is ~ 2-3 μm, which is comparable to that in Areas 4 and 5 during initial material feeding seen in Figs. 6 and 7. Note that the shapes of the micro-ribbons are 3D in nature, so Areas i-iv are not necessarily from the same micro-ribbon. We have thus repeated such characterization for different X-Z cross-sections along the deposition track and have reached the same conclusion: the AA2024 tracer appears similar along the oval with a recrystallized equiaxed grain structure. This suggests that AFSD leads to a uniform microstructure of AA2024 along these curved micro-ribbons.

A closer examination of the microstructures in Areas i-iv reveals that AA6061 generally has a larger grain size and a higher LAB fraction than AA2024 (Figs. 9(f)-(m)), suggesting less complete recrystallization. Within each of these areas, however, the two materials are characterized by almost the same thermomechanical condition. The observed microstructure differences are likely caused by the presence of Cu-based precipitates in AA2024 [62] and Mg-Si precipitates in AA6061 [63]. From previous works on friction stirring of various Al alloys, the original precipitates in the feed material may dissolve, re-precipitate, and coarsen during deposition [23, 24]. Under the AFSD thermomechanical condition, the different kinetics of these processes between Cu-based and Mg-Si precipitates can vitally influence the resultant microstructures, e.g., via pinning of grain boundary migration [64].

In a similar way, we have characterized the microstructure of the micro-ribbons formed by the edge tracer deposition, which are detailed in the *Supplementary Materials*. Uniform along the long arch-shaped micro-ribbons, the microstructure is also characterized by fine, equiaxed grains—similar to those seen at the end of initial material feeding.

5. Discussion

5.1. Quantitative insights into the plastic deformation during AFSD

Throughout the AFSD process, the material undergoes several major deformation steps, including extrusion and torsion during initial material feeding (Section 3.1) and shear-induced thinning during steady-state deposition (Section 3.2). Plastic deformation is history dependent; a rigorous calculation of the total strain requires information about the material shape at all intermediate deformation steps during AFSD, which may necessitate *in situ* X-ray imaging with an ultrahigh-speed detector [65, 66]. That being said, our X-ray computed tomography results still allow for a baseline estimation of the deformation characteristics in AFSD. Here, we perform such estimation based on the measurement of the center tracer dimensions, but using the edge tracer would arrive at similar conclusions.

5.1.1. Strain development during initial material feeding: extrusion- and torsion-like deformation

On the global scale, extrusion happens when the feed material yields and spreads underneath the tool head to form a thin disc. The diameter of this disc is measured as 28.5 mm in this work, which is the same as average track width. The corresponding cross-sectional area is $A_{extrusion} = \frac{1}{4}\pi(28.5)^2 = 637.94\ mm^2$. From Section 2, the cross-sectional area of the feed-rod is $A_{feed-rod} = 90.25\ mm^2$. As illustrated in Fig. 10, the engineering strain along the Z-direction in this extrusion step can be calculated as:

$$\epsilon_z = \frac{A_{feed-rod}}{A_{extrusion}} - 1 = -0.86. \quad (1)$$

Given that the volume stays constant during plastic deformation, we have $(1+\epsilon_x)(1+\epsilon_y)(1+\epsilon_z) = 1$, where the transverse strain ϵ_x and ϵ_y are equal to each other. This gives $\epsilon_x = \epsilon_y = 1.6$. The extrusion step leads to dimension changes and deformation of the center tracer. Before extrusion, the center tracer has an in-plane diameter of $D_0 = 3.175\ mm$. After extrusion, its diameter increases as: $D_1 = D_0\sqrt{\frac{A_{extrusion}}{A_{feed-rod}}} = 8.46\ mm$.

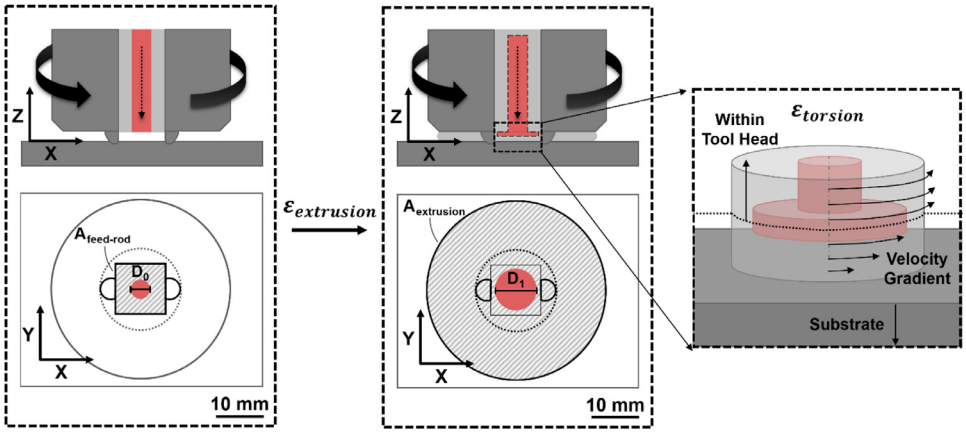

Fig. 10. Strain caused by extrusion and torsion during initial material feeding. Because of material extrusion under the tool head, the in-plane dimensions of the feed-rod and the cylindrical tracer both increase. Torsion is present as a result of the rotation rate gradient from the tool head bottom to the substrate. The red color denotes the AA2024 tracer, while gray denotes the AA6061 matrix.

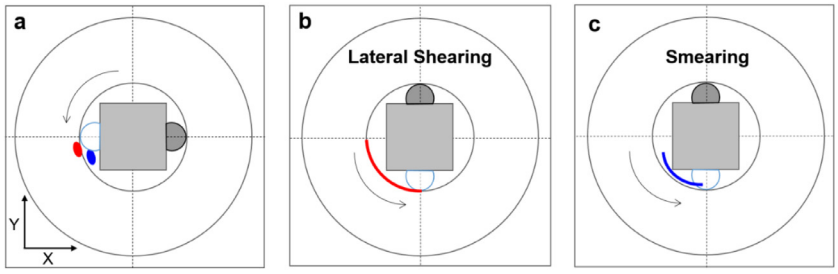

Fig. 11. Possible mechanisms for material thinning during steady-state deposition. A small material volume in (a) can be thinned either by (b) lateral shearing or (c) smearing due to the rotating protrusions and tool head in AFSD.

As discussed in Section 3.1, the center tracer develops torsional strain during initial material feeding because of the rotation rate gradient from Z = 1 mm to Z = 0 mm, which leads to the corkscrew appearance seen in Fig. 3(c). For a given point in the cylindrical tracer, we can take its radial direction as the *x*-direction and the circumferential direction as the *y*-direction to construct a Cartesian coordinate system. The corresponding shear strain can be calculated as [67]:

$$\gamma_{yz} = \mathrm{r}\Delta\theta/h. \tag{2}$$

Here, $\Delta\theta$ is the total twisting angle in radians and h is the deposition thickness. For the scenario in Fig. 3(c), the total twisting angle of the corkscrew is measured as 3π, $h = 1\ mm$, and the outer edge radius is $\mathrm{r} = \frac{3.175\mathrm{mm}}{2} = 1.588\ mm$. This gives a minimum shear strain of 0 in the center (r = 0) and a maximum shear strain of $\gamma_{yz} = \frac{\mathrm{r}\Delta\theta}{h} = \frac{1.588\ mm\times\ 3\pi}{1\ mm} = 14.96$ at the outer edge of the tracer.

When extrusion strain and torsional strain are both present in the tracer material, the equivalent strain ε_e can be calculated as [68]:

$$\varepsilon_e = \int \dot{\varepsilon}_e dt;\ \dot{\varepsilon}_e = \sqrt{\frac{2}{9}\left[(\dot{\varepsilon}_x - \dot{\varepsilon}_y)^2 + (\dot{\varepsilon}_y - \dot{\varepsilon}_z)^2 + (\dot{\varepsilon}_z - \dot{\varepsilon}_x)^2 + \frac{3}{2}\left(\dot{\gamma}_{xy}^2 + \dot{\gamma}_{yz}^2 + \dot{\gamma}_{zx}^2\right)\right]}. \tag{3}$$

Constant volume leads to $d\varepsilon_x + d\varepsilon_y + d\varepsilon_z = 0$, so $d\varepsilon_x = d\varepsilon_y = -\frac{d\varepsilon_z}{2}$. Equation 3 is then reduced to $d\varepsilon_e = \sqrt{\frac{2}{9}[(-\frac{1}{2}d\varepsilon_z - d\varepsilon_z)^2 + (-\frac{1}{2}d\varepsilon_z - d\varepsilon_z)^2 + \frac{3}{2}d\gamma_{yz}{}^2]} = \sqrt{d\varepsilon_z{}^2 + \frac{1}{3}d\gamma_{yz}{}^2}$. Since the shear strain by torsion scales with radius, the equivalent strain reaches maximum at the outer edge of the tracer (at $\mathrm{r} = 1.588\ mm$). At this location, the shear component is dominant; considering it alone, we have $d\varepsilon_e > \frac{d\gamma_{yz}}{\sqrt{3}}$, and $\varepsilon_e > \frac{\gamma_{yz}}{\sqrt{3}} = 8.64$. In other words, the equivalent strain at the center tracer edge is larger than 8.64.

5.1.2. Strain development during steady-state deposition: shear-induced thinning

The micro-ribbon formation in AFSD is probably a result of the material-protrusion interactions, which are analogous to material-pin interactions in FSW [69-71]. From the X-ray tomography observation, the footprint of the micro-ribbons resides well outside of the protrusions' outer radius on the advancing side, rather than resembling the paths of the tool protrusions. As a result, it is unlikely that the micro-ribbon formation is caused by a simple 'tear-off' process. Instead, subsequent deformation by the rotating tool head is necessary to cause elongation and thinning. It is thus reasonable to suggest that the micro-ribbons of tracer material are formed via a multi-step process. This process probably begins with an initial 'tear-off' event that separates a slice of the tracer; after that, compression and shear forces from the protrusions and rotating tool head gradually flatten and elongate the slice.

At least two possible mechanisms contribute to elongation and thinning. First, when the slice of tracer material is on the side of the protrusions (red spot in Fig. 11(a)), the rapid protrusion rotation can effectively shear the material laterally, as illustrated in Fig. 11(b). Second, when the slice of tracer material is below the protrusions (blue spot in Fig. 11(a)), the protrusions and rotating tool head can impose compression and shear to smear the material, causing elongation and thinning. This is illustrated in Fig. 11(c). To quantify the strain accumulation in such shear-induced thinning processes, it is necessary to understand the dimensions and geometry of the slice of the tracer as well as the details of the elongation and thinning steps in forming the micro-ribbon.

Overall, the strain development associated with shear-induced thinning is expected to be important, which is unfortunately challenging to quantify without further information on the micro-ribbon formation process. That being said, we can still conclude that AFSD is a *severe plastic deformation* process because even in the initial material feeding step alone, the outer edge of the center tracer ($\mathrm{r} = 1.588\ mm$) is characterized by a shear strain of 14.96 and an equivalent strain larger than 8.64. Note that the in-plane dimension of the center tracer is only about 1/3 of the feed-rod; at the edge of the feed-rod, the torsional shear strain should be much larger and the equivalent strain is well above the value of 10. Due to the uncounted strain associated with micro-ribbon formation, these values should be taken as lower bounds when estimating the strain in AFSD. Therefore, we may conclude that the total strain in AFSD is generally on the order of 10^1. This conclusion is consistent with previous microstructure characterization results of AA6061 processed by AFSD

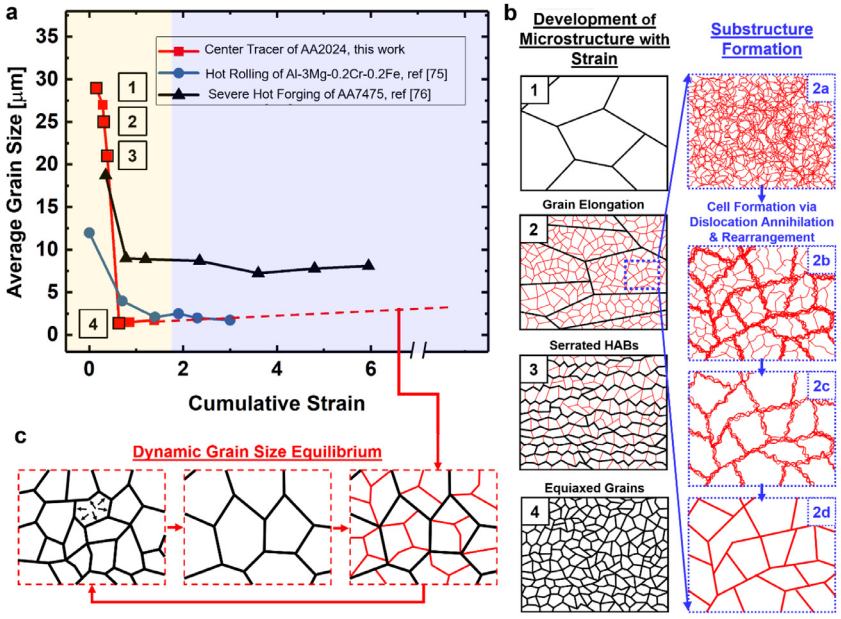

Fig. 12. Quantitative relationship between the grain size and strain. (a) Plot of the data from this work for AA2024, in which the color contrast of the background distinguishes initial material feeding and steady-state deposition. For comparison, also included are the results from hot rolling of Al-3Mg-0.2Cr-0.2Fe [75], and severe hot forging of AA7475 [76]. Illustrations of the dynamic microstructure evolution mechanisms during (b) initial material feeding and (c) steady-state deposition in AFSD of AA2024.

[32], in which a strong C-type shear texture is observed, indicating a shear strain value greater than 10 [72].

5.2. Towards a quantitative relationship between the strain and grain size

From the above strain analysis and previous *in situ* thermal measurement [31], a picture for the co-deformation and dynamic microstructure evolution has become clear. During initial material feeding, the grain size of the center tracer decreases rapidly from tens of microns to a few microns (Figs. 6 and 7). During steady-state deposition, the center tracer undergoes drastic thinning with large strain accumulation. However, the microstructure characterization shows no further grain refinement (Fig. 9). This trend can be better presented by establishing a quantitative relationship between the strain and grain size for the AA2024 center tracer.

During initial material feeding, we focus on the regions analyzed in Figs. 6 and 7, which are along the central rotation axis with minimal torsional effects. The plastic deformation of these regions is mainly caused by uniform compression from the feeding actuator. The associated strain is estimated as follows. Moving down along the central rotation axis, the center tracer can be divided into many small deformed cylindrical volumes labeled 1, 2, 3, … From Volume j to Volume $j+1$, the incremental plastic strain may be represented by $\Delta\varepsilon_{j,j+1} = |ln\frac{A_{j+1}}{A_j}|$, where A_{j+1} and A_j are the average cross-sectional areas of Volume j and Volume $j+1$, respectively. The cumulative strain of the tracer material at a given location (labeled Volume k) can be then estimated as $\varepsilon_k = \sum_{j=1}^{k-1} \Delta\varepsilon_{j,j+1} = \sum_{j=1}^{k-1} |ln\frac{A_{j+1}}{A_j}|$. This approach is inspired by the previous work on cumulative strain estimation in FSW [44].

Using this approach, Fig. 12(a) plots the grain size for the center tracer as a function of the strain during initial material feeding. The grain size initially decreases rapidly with the strain, but it generally stays within the range of 1-2 μm without further reduction once a critical strain level $\varepsilon_{critical} \sim 0.63$ is reached. For the steady-state deposition stage, the grain size is in a comparable range without further grain refinement (as can be seen from Fig. 9); the strain level is higher than that in initial material feeding but the exact value is difficult to quantify. We thus use a dashed line to represent the grain size-strain correlation for steady-state deposition.

The observed relationship between the strain and grain size is consistent with the GDRX mechanism identified in Section 4 (Fig. 8). As the shear strain increases, subgrains form due to dynamic recovery, the grains become elongated and thinner, and the grain size decreases. When a critical strain level is reached ($\varepsilon = \varepsilon_{critical}$), the HAB spacing for elongated grains approaches the subgrain size; the adjacent grain boundaries pinch off, forming a roughly equiaxed microstructure [64, 73, 74]. Upon further deformation ($\varepsilon > \varepsilon_{critical}$), dynamic recovery continues to eliminate dislocations and create subgrain boundaries, which are transformed to LABs and then to HABs. This reduces the grain size. Meanwhile, HAB migration increases the grain size. When the grain size is larger than the subgrain size, substructure pinning inhibits HAB migration; as soon as the grain size is smaller than the subgrain size, HAB migration is accelerated [75]. A dynamic equilibrium between such competing processes is finally reached, so the recrystallized grain size is approximately fixed at the subgrain size level despite additional deformation. The related microstructure evolution processes are illustrated in Figs. 12(b) and (c).

The subgrain size decreases when the strain rate $\dot{\varepsilon}$ increases or the temperature T decreases. AFSD is a complicated process featuring time-dependent thermomechanical conditions. During initial material feeding, the material temperature is expected to be considerably lower than steady-state deposition, as the extensive material flow in the latter can lead to significant volumetric heat generation [31]. This temperature difference may cause a larger value of the Zener-Hollomon parameter (through the exponential relationship), a smaller subgrain size, and therefore a smaller recrystallized grain size in initial material feeding than steady-state deposition—which is consistent with the observations in Figs 6-9.

Along with AFSD of AA2024, we plot the results from hot rolling of Al-3Mg-0.2Cr-0.2Fe [75] and severe hot forging of AA7475 [76] in Fig. 12(a). A similar trend is observed: the grain size has a rapid drop initially, which is followed by a plateau once the strain is above a critical level. For hot rolling of Al-3Mg-0.2Fe, GDRX has also been identified as a major mechanism for grain size reduction. For severe hot forging of AA7475, the grain size is reduced by micro-shear band-based grain subdivision, which is analogous to GDRX: the final grain size is determined by the minimum spacing of micro-shear bands and is weakly dependent on the applied strain for $\varepsilon > \varepsilon_{critical}$. Overall, the grain size trend (with respect to the strain) observed in the three cases in Fig. 12(a) can be viewed as a generic feature of dynamic microstructure evolution dominated by continuous recrystallization, which typically occurs during large deformation of high stacking fault energy materials like Al

alloys [59, 64]. We acknowledge the possibility of grain growth during cooling after AFSD, which may slightly modify the grain size data; however, this is not likely to affect the main trend observed here.

6. Conclusions and future perspectives

As demonstrated by AFSD in this work, metal additive manufacturing can be implemented via severe plastic deformation instead of melting and solidification, in which the feed material is characterized by drastic shape change on the mesoscopic level and concurrent grain refinement. Through X-ray computed tomography and microstructure characterization of tracer-based feed-rods, we have systematically investigated the fundamentals of plastic deformation in AFSD, wherein the most significant findings include:

- During initial material feeding, the material is deformed due to extrusion and torsion. The former occurs when the feed-rod is compressed and transformed to a thin disc; the latter is caused by the rotation rate gradient along the vertical direction. In this processing step, the grain size of the AA2024 tracer quickly decreases from 25-30 μm to 1-2 μm via GDRX.
- During steady-state deposition, the material is severely thinned probably due to material-protrusion interactions, and the original cylindrical center and edge tracers are transformed into micro-ribbons piling up along the deposition track. In this processing step, despite large strain accumulation, no further grain refinement is observed because of the dynamic equilibrium of various competing processes.
- We analyze the deformation steps in AFSD and estimate the magnitude of strain components associated with extrusion, torsion, and shear-induced thinning. We conclude that AFSD is a hot, severe plastic deformation process with the strain generally being on the order of 10^1.
- We establish a quantitative relationship between the grain size and strain for AFSD of AA2024. This includes an initial rapid drop of the grain size followed by a plateau as the strain increases above a critical level. This trend is consistent with the identified GDRX mechanism from microstructural analysis, and is similar to that observed in hot forging and hot rolling of other Al alloys.

The conclusions drawn from this work are based on Al alloys, which have high stacking fault energy and flow sufficiently under the rotating tool head [31, 32]. For materials with medium and low stacking fault energy, GDRX is not necessarily the dominant recrystallization mechanism, which will likely affect the microstructure uniformity and the grain size trend with respect to the strain [59]. For materials with poor sticking to the tool head, the material flow may not be as sufficient so that the total strain magnitude could be lower. These unexplored areas provide plenty of opportunities for the next-phase research and development of the process.

This work is motivated by the deformation nature of AFSD: all the material domains in the feed-rod undergo high-temperature, severe plastic deformation and dynamic recrystallization, resulting in fully-dense material and excellent mechanical properties in the as-printed state. Such salient advantages may trigger the development of other deformation processing-based additive technologies by future researchers, who may find the methodology and conclusions of this work useful.

Declaration of Competing Interest

The authors declare that they have no known competing financial interests or personal relationships that could have appeared to influence the work reported in this paper.The authors declare the following financial interests/personal relationships which may be considered as potential competing interests.

Acknowledgement

HZY and JMS acknowledge the support from Virginia Tech-ARL CRADA (#16-13). HZY would also like to acknowledge the support from the Department of Materials Science and Engineering at Virginia Tech. MEJP would like to acknowledge the support by the National Science Foundation Graduate Research Fellowship Program—any opinions, findings, and conclusions or recommendations expressed in this material are those of the authors and do not necessarily reflect the views of the National Science Foundation.

Supplementary materials

Supplementary material associated with this article can be found, in the online version, at doi:10.1016/j.mtla.2021.101159.

References

[1] S.S. Babu, L. Love, R. Dehoff, W. Peter, T.R. Watkins, S. Pannala, Additive manufacturing of materials: Opportunities and challenges, MRS Bull. 40 (12) (2015) 1154–1161.
[2] W.J. Sames, F.A. List, S. Pannala, R.R. Dehoff, S.S. Babu, The metallurgy and processing science of metal additive manufacturing, Int. Mater. Rev. 61 (5) (2016) 315–360.
[3] W.E. Frazier, Metal additive manufacturing: a review, J. Mater. Eng. Perform. 23 (6) (2014) 1917–1928.
[4] A. du Plessis, I. Yadroitsava, I. Yadroitsev, Effects of defects on mechanical properties in metal additive manufacturing: a review focusing on X-ray tomography insights, Mater. Design 187 (2020) 108385.
[5] S.A. Khairallah, A.T. Anderson, A. Rubenchik, W.E. King, Laser powder-bed fusion additive manufacturing: physics of complex melt flow and formation mechanisms of pores, spatter, and denudation zones, Acta Mater. 108 (2016) 36–45.
[6] C. Li, Z.Y. Liu, X.Y. Fang, Y.B. Guo, Residual stress in metal additive manufacturing, Procedia CIRP 71 (2018) 348–353.
[7] Z. Yan, W. Liu, Z. Tang, X. Liu, N. Zhang, M. Li, H. Zhang, Review on thermal analysis in laser-based additive manufacturing, Opt. Laser Technol. 106 (2018) 427–441.
[8] A. Basak, S. Das, Epitaxy and microstructure evolution in metal additive manufacturing, Annu. Rev. Mater. Res. 46 (1) (2016) 125–149.
[9] S.L. Sing, W.Y. Yeong, Laser powder bed fusion for metal additive manufacturing: perspectives on recent developments, Virtual Phys. Prototyping 15 (3) (2020) 359–370.
[10] Z.Y. Liu, C. Li, X.Y. Fang, Y.B. Guo, Energy consumption in additive manufacturing of metal parts, Proc. Manuf. 26 (2018) 834–845.
[11] F.C. Campbell, Chapter 16: deformation processing, in: F.C. Campbell (Ed.), in: Elements of Metallurgy and Engineering Alloys, ASM International, 2008, pp. 279–302.
[12] N. Tuncer, A. Bose, Solid-state metal additive manufacturing: a review, JOM 72 (9) (2020) 3090–3111.
[13] M. Srivastava, S. Rathee, S. Maheshwari, A. Noor Siddiquee, T.K. Kundra, A review on recent progress in solid state friction based metal additive manufacturing: friction stir additive techniques, Crit. Rev. Solid State Mater. Sci. 44 (5) (2019) 345–377.
[14] A. Bournias-Varotsis, X. Han, R.A. Harris, D.S. Engstrøm, Ultrasonic additive manufacturing using feedstock with build-in circuitry for 3D metal embedded electronics, Additive Manuf. 29 (2019) 100799.
[15] A. Hehr, M. Norfolk, A comprehensive review of ultrasonic additive manufacturing, Rapid Prototyp. J. 26 (3) (2019) 445–458.
[16] N. Sridharan, M.N. Gussev, C.M. Parish, D. Isheim, D.N. Seidman, K.A. Terrani, S.S. Babu, Evaluation of microstructure stability at the interfaces of Al-6061 welds fabricated using ultrasonic additive manufacturing, Mater. Charact. 139 (2018) 249–258.
[17] S. Pathak, G.C. Saha, Development of sustainable cold spray coatings and 3D additive manufacturing components for repair/manufacturing applications: a critical review, Coatings 7 (8) (2017) 122.
[18] X. Wang, F. Feng, M.A. Klecka, M.D. Mordasky, J.K. Garofano, T. El-Wardany, A. Nardi, V.K. Champagne, Characterization and modeling of the bonding process in cold spray additive manufacturing, Add. Manuf. 8 (2015) 149–162.
[19] S. Yin, P. Cavaliere, B. Aldwell, R. Jenkins, H. Liao, W. Li, R. Lupoi, Cold spray additive manufacturing and repair: fundamentals and applications, Add. Manuf. 21 (2018) 628–650.
[20] R.J. Griffiths, M.E.J. Perry, J.M. Sietins, Y. Zhu, N. Hardwick, C.D. Cox, H.A. Rauch, H.Z. Yu, A perspective on solid-state additive manufacturing of aluminum matrix composites using MELD, J. Mater. Eng. Perform. 28 (2) (2019) 648–656.
[21] H.Z. Yu, M.E. Jones, G.W. Brady, R.J. Griffiths, D. Garcia, H.A. Rauch, C.D. Cox, N. Hardwick, Non-beam-based metal additive manufacturing enabled by additive friction stir deposition, Scr. Mater. 153 (2018) 122–130.
[22] M.E.J. Perry, R.J. Griffiths, D. Garcia, J.M. Sietins, Y. Zhu, H.Z. Yu, Morphological and microstructural investigation of the non-planar interface formed in solid-state metal additive manufacturing by additive friction stir deposition, Add. Manuf. 35 (2020) 101293.
[23] B.J. Phillips, D.Z. Avery, T. Liu, O.L. Rodriguez, C.J.T. Mason, J.B. Jordon, L.N. Brewer, P.G. Allison, Microstructure-deformation relationship of additive friction stir-deposition Al–Mg–Si, Materialia 7 (2019) 100387.

[24] O.G. Rivera, P.G. Allison, L.N. Brewer, O.L. Rodriguez, J.B. Jordon, T. Liu, W.R. Whittington, R.L. Martens, Z. McClelland, C.J.T. Mason, L. Garcia, J.Q. Su, N. Hardwick, Influence of texture and grain refinement on the mechanical behavior of AA2219 fabricated by high shear solid state material deposition, Mater. Sci. Eng. 724 (2018) 547–558.
[25] C.J.T. Mason, R.I. Rodriguez, D.Z. Avery, B.J. Phillips, B.P. Bernarding, M.B. Williams, S.D. Cobbs, J.B. Jordon, P.G. Allison, Process-structure-property relations for As-deposited solid-state additively manufactured high-strength aluminum alloy, Additive Manuf. (2021) 101879.
[26] J.K. Yoder, R.J. Griffiths, H.Z. Yu, Deformation-based additive manufacturing of 7075 aluminum with wrought-like mechanical properties, Mater. Design 198 (2021) 109288.
[27] O.G. Rivera, P.G. Allison, J.B. Jordon, O.L. Rodriguez, L.N. Brewer, Z. McClelland, W.R. Whittington, D. Francis, J. Su, R.L. Martens, N. Hardwick, Microstructures and mechanical behavior of Inconel 625 fabricated by solid-state additive manufacturing, Mater. Sci. Eng. 694 (2017) 1–9.
[28] J.R. Calvert, Microstructure and mechanical properties of WE43 alloy produced via additive friction stir technology, Materials Science and Engineering, Virginia Polytechnic Institute and State University, Blacksburg, VA, 2015.
[29] H.Z. Yu, R.S. Mishra, Additive friction stir deposition: a deformation processing route to metal additive manufacturing, Mater. Res. Lett. 9 (2) (2021) 71–83.
[30] R.S. Mishra, Z.Y. Ma, Friction stir welding and processing, Mater. Sci. Eng. 50 (1) (2005) 1–78.
[31] D. Garcia, W.D. Hartley, H.A. Rauch, R.J. Griffiths, R. Wang, Z.J. Kong, Y. Zhu, H.Z. Yu, In situ investigation into temperature evolution and heat generation during additive friction stir deposition: a comparative study of Cu and Al-Mg-Si, Add. Manuf. 34 (2020) 101386.
[32] R.J. Griffiths, D. Garcia, J. Song, V.K. Vasudevan, M.A. Steiner, W. Cai, H.Z. Yu, Solid-state additive manufacturing of aluminum and copper using additive friction stir deposition: Process-microstructure linkages, Materialia 15 (2021) 100967.
[33] Y. Han, R.J. Griffiths, H.Z. Yu, Y. Zhu, Quantitative microstructure analysis for solid-state metal additive manufacturing via deep learning, J. Mater. Res. (2020) 1–13.
[34] J.L. Priedeman, B.J. Phillips, J.J. Lopez, B.E. Tucker Roper, B.C. Hornbuckle, K.A. Darling, J.B. Jordon, P.G. Allison, G.B. Thompson, Microstructure development in additive friction stir-deposited Cu, Metals 10 (11) (2020) 1538.
[35] D.Z. Avery, B.J. Phillips, C.J.T. Mason, M. Palermo, M.B. Williams, C. Cleek, O.L. Rodriguez, P.G. Allison, J.B. Jordon, Influence of grain refinement and microstructure on fatigue behavior for solid-state additively manufactured Al-Zn-Mg-Cu alloy, Metall. Mater. Trans. A 51 (6) (2020) 2778–2795.
[36] D.Z. Avery, O.G. Rivera, C.J.T. Mason, B.J. Phillips, J.B. Jordon, J. Su, N. Hardwick, P.G. Allison, Fatigue behavior of solid-state additive manufactured inconel 625, JOM 70 (11) (2018) 2475–2484.
[37] Z. McClelland, D.Z. Avery, M.B. Williams, C.J.T. Mason, O.G. Rivera, C. Leah, P.G. Allison, J.B. Jordon, R.L. Martens, N. Hardwick, in: Microstructure and Mechanical Properties of High Shear Material Deposition of Rare Earth Magnesium Alloys WE43, Springer International Publishing, Cham, 2019, pp. 277–282.
[38] B.A. Rutherford, D.Z. Avery, B.J. Phillips, H.M. Rao, K.J. Doherty, P.G. Allison, L.N. Brewer, J.B. Jordon, Effect of thermomechanical processing on fatigue behavior in solid-state additive manufacturing of Al-Mg-Si alloy, Metals 10 (7) (2020) 947.
[39] K. Anderson-Wedge, D. Avery, S.R. Daniewicz, J.W. Sowards, P. Allison, J. Jordon, R.L. Amaro, Characterization of the fatigue behavior of additive friction stir-deposition AA2219, Int. J. Fatigue 142 (2021) 105951.
[40] R.J. Griffiths, D.T. Petersen, D. Garcia, H.Z. Yu, Additive friction stir-enabled solid-state additive manufacturing for the repair of 7075 aluminum alloy, Appl. Sci. 9 (17) (2019) 3486.
[41] W.D. Hartley, D. Garcia, J.K. Yoder, E. Poczatek, J.H. Forsmark, S.G. Luckey, D.A. Dillard, H.Z. Yu, Solid-state cladding on thin automotive sheet metals enabled by additive friction stir deposition, J. Mater. Process. Technol. (2021) 117045.
[42] J.B. Jordon, P.G. Allison, B.J. Phillips, D.Z. Avery, R.P. Kinser, L.N. Brewer, C. Cox, K. Doherty, Direct recycling of machine chips through a novel solid-state additive manufacturing process, Mater. Design 193 (2020) 108850.
[43] A. Gerlich, P. Su, M. Yamamoto, T.H. North, Effect of welding parameters on the strain rate and microstructure of friction stir spot welded 2024 aluminum alloy, J. Mater. Sci. 42 (14) (2007) 5589–5601.
[44] X.C. Liu, Y.F. Sun, T. Nagira, K. Ushioda, H. Fujii, Experimental evaluation of strain and strain rate during rapid cooling friction stir welding of pure copper, Sci. Technol. Weld. Join. 24 (4) (2019) 352–359.
[45] F.C. Liu, Y. Hovanski, M.P. Miles, C.D. Sorensen, T.W. Nelson, A review of friction stir welding of steels: tool, material flow, microstructure, and properties, J. Mater. Sci. Technol. 34 (1) (2018) 39–57.
[46] I.J. Beyerlein, C.N. Tomé, Analytical modeling of material flow in equal channel angular extrusion (ECAE), Mater. Sci. Eng. 380 (1) (2004) 171–190.
[47] J.J. Jonas, C. Ghosh, L.S. Toth, The equivalent strain in high pressure torsion, Mater. Sci. Eng. 607 (2014) 530–535.
[48] R.Z. Valiev, T.G. Langdon, Principles of equal-channel angular pressing as a processing tool for grain refinement, Prog. Mater Sci. 51 (7) (2006) 881–981.
[49] A. Vinogradov, Y. Estrin, Analytical and numerical approaches to modelling severe plastic deformation, Prog. Mater Sci. 95 (2018) 172–242.
[50] Y. Zhu, K. Ameyama, P.M. Anderson, I.J. Beyerlein, H. Gao, H.S. Kim, E. Lavernia, S. Mathaudhu, H. Mughrabi, R.O. Ritchie, N. Tsuji, X. Zhang, X. Wu, Heterostructured materials: superior properties from hetero-zone interaction, Mater. Res. Lett. 9 (1) (2021) 1–31.
[51] Y. Estrin, Y. Beygelzimer, R. Kulagin, Design of architectured materials based on mechanically driven structural and compositional patterning, Adv. Eng. Mater. 21 (9) (2019) 1900487.
[52] H.N.B. Schmidt, T.L. Dickerson, J.H. Hattel, Material flow in butt friction stir welds in AA2024-T3, Acta Mater. 54 (4) (2006) 1199–1209.
[53] Y. Morisada, H. Fujii, Y. Kawahito, K. Nakata, M. Tanaka, Three-dimensional visualization of material flow during friction stir welding by two pairs of X-ray transmission systems, Scr. Mater. 65 (12) (2011) 1085–1088.
[54] Q. Yang, S. Mironov, Y.S. Sato, K. Okamoto, Material flow during friction stir spot welding, Mater. Sci. Eng. 527 (16) (2010) 4389–4398.
[55] S. Mukherjee, A.K. Ghosh, Flow visualization and estimation of strain and strain-rate during friction stir process, Mater. Sci. Eng. 527 (20) (2010) 5130–5135.
[56] T.U. Seidel, A.P. Reynolds, Visualization of the material flow in AA2195 friction–stir welds using a marker insert technique, Metall. Mater. Trans. A 32 (11) (2001) 2879–2884.
[57] M.M. Corporation, Meld Manufacturing, 2021. http://meldmanufacturing.com/.
[58] MACKENZIE J.K., Second paper on statistics associated with the random disorientation of cubes, Biometrika 45 (1-2) (1958) 229–240.
[59] T. Sakai, A. Belyakov, R. Kaibyshev, H. Miura, J.J. Jonas, Dynamic and post-dynamic recrystallization under hot, cold and severe plastic deformation conditions, Prog. Mater Sci. 60 (2014) 130–207.
[60] A.D. Rollett, G.S. Rohrer, F.J. Humphreys, Chapter 13 - Hot Deformation and Dynamic Restoration, Recrystallization and Related Annealing Phenomena, Third Edition, Elsevier, 2017.
[61] U. Suhuddin, S. Mironov, H. Krohn, M. Beyer, J.F. Dos Santos, Microstructural evolution during friction surfacing of dissimilar aluminum alloys, Metall. Mater. Trans. A 43 (13) (2012) 5224–5231.
[62] J.L. García-Hernández, C.G. Garay-Reyes, I.K. Gómez-Barraza, M.A. Ruiz-Esparza-Rodríguez, E.J. Gutiérrez-Castañeda, I. Estrada-Guel, M.C. Maldonado-Orozco, R. Martínez-Sánchez, Influence of plastic deformation and Cu/Mg ratio on the strengthening mechanisms and precipitation behavior of AA2024 aluminum alloys, J. Mater. Res. Technol. 8 (6) (2019) 5471–5475.
[63] W. Miao, D. Laughlin, Precipitation hardening in aluminum alloy 6022, Scr. Mater. 40 (7) (1999) 873–878.
[64] A.D. Rollett, G.S. Rohrer, F.J. Humphreys, Chapter 14 - Continuous Recrystallization During and after Large Strain Deformation, Recrystallization and Related Annealing Phenomena, Third Edition, Elsevier, 2017.
[65] R. Cunningham, C. Zhao, N. Parab, C. Kantzos, J. Pauza, K. Fezzaa, T. Sun, A.D. Rollett, Keyhole threshold and morphology in laser melting revealed by ultrahigh-speed x-ray imaging, Science 363 (6429) (2019) 849.
[66] C. Zhao, K. Fezzaa, R.W. Cunningham, H. Wen, F. De Carlo, L. Chen, A.D. Rollett, T. Sun, Real-time monitoring of laser powder bed fusion process using high-speed X-ray imaging and diffraction, Sci. Rep. 7 (1) (2017) 3602.
[67] A.P. Zhilyaev, T.G. Langdon, Using high-pressure torsion for metal processing: Fundamentals and applications, Prog. Mater Sci. 53 (6) (2008) 893–979.
[68] G.E. Dieter, Mechanical metallurgy, McGraw-Hill, New York, 1986.
[69] R. Beygi, M.Z. Mehrizi, D. Verdera, A. Loureiro, Influence of tool geometry on material flow and mechanical properties of friction stir welded Al-Cu bimetals, J. Mater. Process. Technol. 255 (2018) 739–748.
[70] M. Guerra, C. Schmidt, J.C. McClure, L.E. Murr, A.C. Nunes, Flow patterns during friction stir welding, Mater. Charact. 49 (2) (2002) 95–101.
[71] G.K. Padhy, C.S. Wu, S. Gao, Friction stir based welding and processing technologies - processes, parameters, microstructures and applications: a review, J. Mater. Sci. Technol. 34 (1) (2018) 1–38.
[72] G.R. Canova, U.F. Kocks, J.J. Jonas, Theory of torsion texture development, Acta Metall. 32 (2) (1984) 211–226.
[73] W. Blum, Q. Zhu, R. Merkel, H.J. McQueen, Geometric dynamic recrystallization in hot torsion of Al-5Mg-0.6Mn (AA5083), Mater. Sci. Eng. 205 (Issues 1–2) (1996) 23–30 Volume.
[74] K. Huang, R.E. Logé, A review of dynamic recrystallization phenomena in metallic materials, Mater. Design 111 (2016) 548–574.
[75] A. Gholinia, F.J. Humphreys, P.B. Prangnell, Production of ultra-fine grain microstructures in Al–Mg alloys by coventional rolling, Acta Mater. 50 (18) (2002) 4461–4476.
[76] O. Sitdikov, T. Sakai, A. Goloborodko, H. Miura, R. Kaibyshev, Grain refinement in coarse-grained 7475 Al alloy during severe hot forging, Philos. Mag. 85 (11) (2005) 1159–1175.